Plasticity enhancement in metallic glasses via aging-assisted ultrasonic vibrations

Jianyu Chen[1], Shuai Ren[1,2,*], Zhe Chen[1], Jie Dong[1,2], Zhichao Lu[3], Jiahua Zhu[4], Lixing Zhu[1], Yangguang Zhan[1], Xingran Zhao[1], Wenxue Wang[1], Shenghao Zeng[1], Jing Xiao[1], Sajad Sohrabi[1,2], Xiong Liang[1,2], Ke Yang[5], Dong Ma[3] and Jiang Ma[1,2,*] (ID)

[1] State Key Laboratory of Radio Frequency Heterogeneous Integration, Shenzhen University, Shenzhen 518060, People's Republic of China
[2] Shenzhen Key Laboratory of High Performance Nontraditional Manufacturing, College of Mechatronics and Control Engineering, Shenzhen University, Shenzhen 518060, People's Republic of China
[3] Neutron Science Center, Songshan Lake Materials Laboratory, Dongguan, Guangdong 523808, People's Republic of China
[4] School of Materials Science and Engineering, Fujian University of Technology, Fuzhou 350118, People's Republic of China
[5] Shanghai Advanced Research Institute, Chinese Academy of Sciences, Shanghai 201210, People's Republic of China

E-mail: ren.shuai@ylab.ac.cn and majiang@szu.edu.cn

CrossMark

Abstract

The aging of glassy materials is an inevitable process leading to progressive property degradation. In metallic glasses (MGs), aging-induced property degradation poses a persistent challenge to their applications. Over the years, rejuvenating or even reversing the aged glasses remains a critical elusive goal. Here we report that ultrasonic vibration (UV) treatment can reverse aging in a Zr-based MG within 0.5 s, achieving plasticity up to 14.5% that is 1.5 times that of the as-cast MG. This intriguing plasticity enhancement results from a UV-induced higher-energy state, as evidenced by structural enthalpy recovery, boson peak restoration, and a more disordered structure revealed by the pair distribution functions. This higher-energy state can be properly explained through the framework of 'anti-free volume defects' with a high atomic packing density. Furthermore, we propose a novel 'aging-assisted UV loading' method: pre-aging stabilizes the MG, enabling subsequent UV to amplify plasticity. This strategy achieves exceptional plasticity improvement, demonstrating that controlled aging can paradoxically enhance material properties.

---

* Authors to whom any correspondence should be addressed.

1. Introduction

Glassy materials, including amorphous polymers, oxide glasses, and metallic glasses (MGs), generally undergo structural relaxation over time. This time-dependent evolution is known as the aging effect, which originates from the intrinsic thermodynamic metastable stability of these amorphous systems, so that the initial state can transition toward a more stable state with time [1]. While the relaxation process primarily occurs at the local structure level, it can lead to changes in macroscopic properties, resulting in significant performance deterioration. This is particularly evident in the case of MGs, which are considered as a prototype of structural glasses due to their relatively simple atomic packing, also known as amorphous alloys [2–4].

MGs are fabricated by quenching glass-forming metallic liquids at relatively high cooling rates to prevent crystallization [5, 6]. Owing to their unique amorphous structure, MGs exhibit superior properties such as large elastic limits, high strength, good wear resistance, and remarkable soft magnetic properties [7–9]. However, their inherent brittleness has limited their applications. Considerable efforts have been made to enhance the plasticity of MGs through various approaches, such as composition modifications [10], external pressure application [11], and the introduction of nano-scale structure [12]. In particular, Liu *et al* have successfully developed bulk MGs that exhibit both ultra-high plasticity and ultra-high strength at room temperature [13]. As a result, the plasticity of MGs has been significantly improved, which helps to expand their application range.

Unfortunately, the aging effect poses a significant challenge for the applications of MGs. Like other glassy materials, MGs undergo continuous aging in the natural environment. Moreover, shaping MGs into desired components often involves thermo-plastic deformation, which requires heating the sample to the supercooled liquid region. However, this heating process significantly exacerbates the aging effect, leading to a rapid deterioration in properties, particularly in terms of plasticity. This greatly restricts their processing and applications [14]. Therefore, finding ways to mitigate the effect caused by aging is a critical challenge in this field.

Extensive attempts have been made to address this problem and reverse the aging effect in MGs by thermomechanical approaches, such as rejuvenation by elastic loading [15], cryogenic thermal cycling [16], ion irradiation [17], and severe plastic deformation [18, 19]. For example, Pan *et al* [20, 21] have used constrained compression loading to induce substantial plastic flow in a zirconium-based BMG, leading to rejuvenation and strain-hardening. In addition, non-affine thermal strain induced by thermal cycling between room temperature and liquid nitrogen temperature can also lead to significant

changes in the local atomic structure [16]. However, these techniques are often time-consuming, expensive, and operationally cumbersome; more importantly, these methods cannot restore the plasticity of over-aged MGs [22], posing a challenge in practical applications. Therefore, there is an urgent and critical need to develop a fast, simple and efficient method for reversing the aging of MGs, thereby regaining their plasticity.

Recently, it has been found that ultrasonic vibration (UV) loading can effectively soften MGs, leading to a pronounced UV-induced plasticity (UVIP) [23–28]. The mechanism of the softening effect is related to the excitation of flow units (or soft zones) induced by UV loading, which is mainly linked to the localized relaxation processes in MGs [24, 28–30]. Meanwhile, studies have shown that mechanical oscillations can soften and rejuvenate MGs [31, 32]. These findings suggest that UV loading is an effective technique for rejuvenating aged MGs. However, the mechanical properties of the aged samples after UV treatment have not been studied. More importantly, La-based MGs exhibits significant UVIP and rejuvenation at the same time. The deformation during UV loading renders a challenge to determine the exact origin of rejuvenation as being either substantial shear deformation or UVs. Therefore, the underlying mechanisms of UV-induced rejuvenation in the MGs remain an open question.

In this study, we report that UV loading can rapidly reverse aging and restore excellent plasticity in MGs within 0.5 s. Using the as-cast $Zr_{62}Cu_{15.5}Ni_{12.5}Al_{10}$ (Zr62) MG with a plasticity of 9.6%, we accelerated the aging process by annealing the samples at the glass transition temperature (T_g), mimicking the thermoplastic deformation. After aging, the samples lost their compressive plasticity, but after being subjected to UV loading, the samples exhibited a significant recovery in mechanical performance, reaching a large plasticity of 14.5%. The plasticity recovery is found to align with the strong restoration of structural enthalpy and boson peak (BP), as well as the more disordered structure revealed by the pair distribution functions. Negligible structural anisotropy was found, indicating that the rejuvenation is induced by UV, instead of plastic deformation. A framework of 'anti-free volume defects' was introduced, which provides a plausible interpretation of our experimental results. This work presents a fast and simple method to reverse the aging effect of MGs. More importantly, a method of 'aging-assisted UV loading' was proposed, which could be a viable recipe to enhance the properties of MGs.

2. Methods

In this work, the $Zr_{62}Cu_{15.5}Ni_{12.5}Al_{10}$ (at.%) alloy (abbreviated as Zr62 hereafter) was synthesized by arc melting pure Zr

(99.9 at.%), Cu (99.999 at.%), Ni (99.999 at.%), and Al (99.999 at.%) in a high purity argon atmosphere. The ingots were cast into cylindrical rods with a diameter of 2 mm by means of a water-cooled copper mold. The samples were sealed in quartz tubes to prevent oxidation during annealing. The samples were held at a temperature in a box furnace for different periods of time. After that, the samples were cooled down to room temperature in air.

The ultrasonic sonotrode was made of cemented carbide (TC4 titanium alloy) and was combined with a booster and transducer (figure 1), which converted the electrical signals into high frequency vibrations. Therefore, the sonotrode can apply mechanical vibrations perpendicular to the sample under the set pressure. The vibration frequency is 20 000 Hz (with a frequency tolerance range of $\pm$500 Hz), which is a characteristic inherent to the ultrasonic instrument. The instrument permits operation in two control modes: time-control and energy-control. In this work, we used the energy-control mode. The stress was measured by a force gauge located at the base of the sample.

The phase structure of the samples was examined using x-ray diffraction of Cu K α radiation (XRD, Rigaku MiniFlex 600). The thermal properties of the samples were determined using differential scanning calorimetry (DSC, Perkin Elmer DSC-8000) at a heating rate of 20 K min^{-1}. The micromorphology of the samples was characterized using transmission electron microscopy (TEM, FEI F30). The morphology was captured using a field emission scanning electron microscope (SEM) (FEI QUANTA FEG 450). The specific heat of the samples was measured in a physical property measurement system (PPMS 6000) from quantum design through a thermal relaxation method from 2 to 300 K. Macroscopic compression tests were conducted at a strain rate of 5×10^{-4} s^{-1} using a Zwick Z050 testing machine. At least three independent samples were repeated at each condition for data reliability. The samples were cylindrical rods with a height of 4 mm and a diameter of 2 mm. All samples were polished to a mirror finish.

A part of the contact ultrasonic sonotrode was cut off and spliced into a sample, for the x-ray measurements. High-energy x-ray scattering experiments were performed at the BL12SW beamline of the Shanghai synchrotron radiation facility (SSRF) [33]. A beam with an energy of 112 keV and size of 0.5×0.5 mm was used. Each sample data collection time was 60 s. Calibration was performed using a CeO$_2$ NIST powder standard. Diffraction was performed in a transmission mode by using a two-dimensional (2D) detector (Pilatus3 X CdTe 2M). The one-dimensional diffraction patterns were obtained by integrating the 2D diffraction images using GSASII software [34]. The total scattering factor S(Q) and pair-distribution functions G(r) were obtained using PDFgetX3 software package [35].

3. Results and discussion

The DSC curves of the Zr62 sample annealed at T_{g} (653 K) for different times are shown in figure 1(a). A schematic diagram of the annealing process of MGs is given in the inset of figure 1(a). To accelerate the aging process, the samples were sealed and heated up to T_{g} for different aging times and then cooled down to room temperature. A broad exothermic peak below T_{g} is found in the DSC curve of the as-cast sample, corresponding to an irreversible structural relaxation with the annihilation of excess free volume or other structural defects [36]. As the annealing time increases, this broad exothermic peak gradually disappears, accompanied by the reduction of structural relaxation enthalpy (ΔH_{rel}). The sub-T_{g} signal finally disappears when the annealing time is longer than 1 h, and an overshoot above T_{g} appears when the time is above 10 min. These results are consistent with previous work [36]. The as-cast and annealed samples are fully amorphous. (Structure data of all the samples are shown in suppl. figures S1 and S2).

The stress–strain curves of as-cast and aged Zr62 MGs are shown in figure 1(b), which were measured at a strain rate of 5×10^{-4} s^{-1}. (Summary of the mechanical properties and structure relaxation enthalpy (ΔH_{rel}) of the aged samples is shown in suppl. table S1). The as-cast MGs exhibit a compressive plasticity of 9.6% and a strength of 1.55 GPa. As the annealing time increases, the plasticity gradually decreases. The plasticity finally disappears, and the strength decreases to 1.49 GPa when the annealing time is 10 h. Therefore, we took the samples annealed for 10 h as the initial samples subjected to UV treatment.

To investigate the effects of UV loading on aged MGs, UV loading was applied to the well-annealed MGs, and the property evolution under different UV loading conditions was studied. A schematic diagram of UV loading is shown in figure 1(c). The ultrasonic horn moves downward at a uniform rate, contacts the sample, and imposes a compressive force on the sample. The sample processing procedure is shown in figure 1(d). We applied UVs on one side of the sample with a certain ultrasonic energy. To achieve a uniform UV processing effect, the sample was then flipped over and UV were applied on the other side with the same energy. Therefore, each side of the sample was treated with the same energy levels, including 75 J, 100 J and 125 J, respectively (abbreviated as UV-75J, UV-100J, UV-125J hereafter). To ensure the accuracy of the compressive stress–strain curve measurement, the upper and lower surfaces of the cylindrical sample were polished to make them parallel and smooth. The photos in figure 1(d) exhibit the shape of the samples at each stage. Figures 1(e) and (f) present the stress and temperature change during UV loading (with vibration amplitudes of 35.5 μm). With the increase in the input energy, the UV loading time increases, accompanied with the increase in the loading stress maximum. It is evident that the loading stress is generally low (<30 MPa) and the temperature increases but is far below T_{g}. The loading time is as short as around 0.5 s, indicating that UV loading is an efficient method to treat the sample.

We also investigated the influence of vibration amplitude. The amplitude maximum of the ultrasonic instrument is 44.4 μm, which can also be adjusted. Thus, we tested the thermal behaviors of the samples under UV loading with different vibration amplitudes. The DSC results are shown in
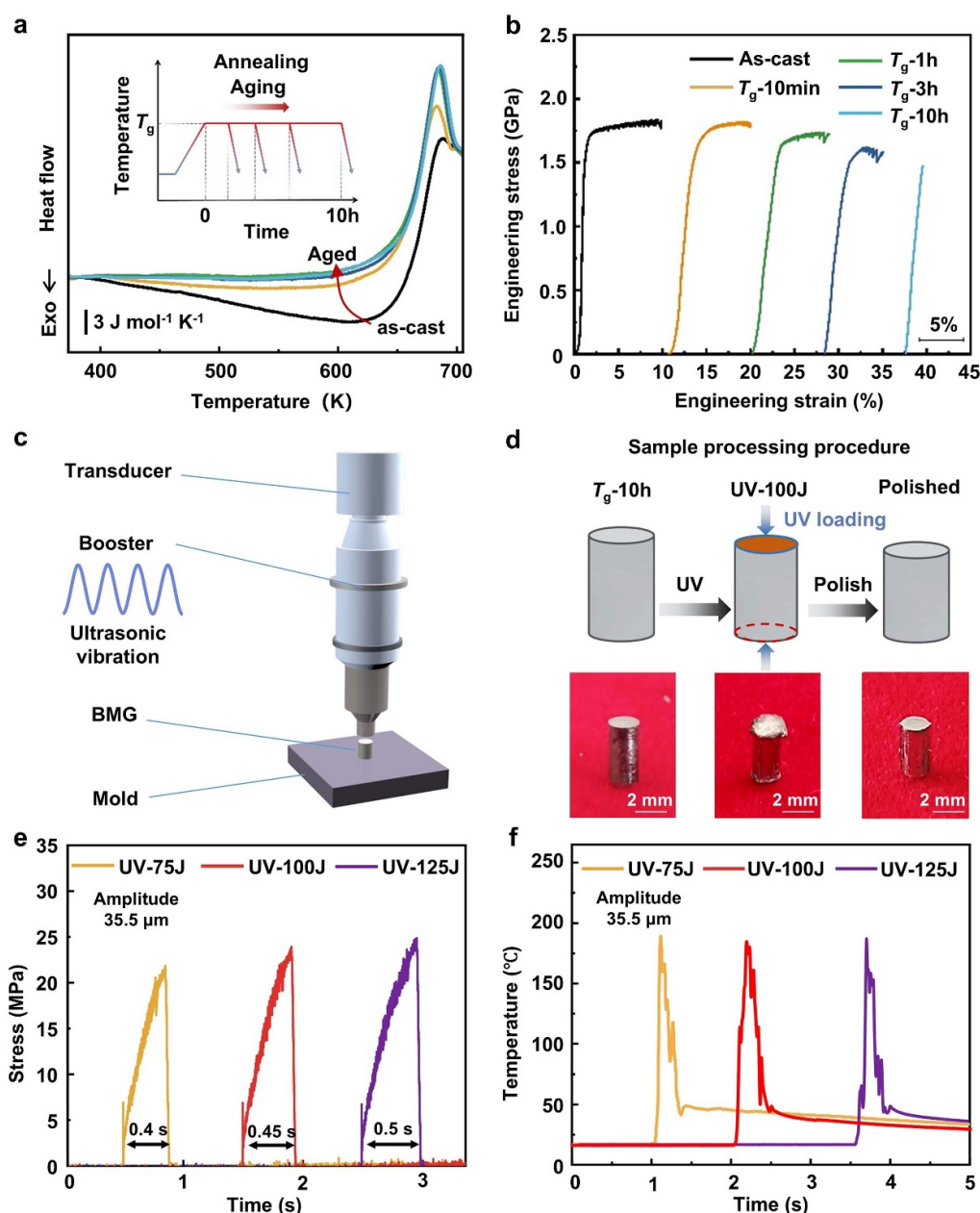
Figure 1. Property changes of Zr62 aged MGs and UV loading process. (a) DSC plots of alloys aged at T_g for different times. The red arrow shows that the reduction of structural relaxation enthalpy as the aging time increases. Inset: schematic diagram of the annealing process of MGs. (b) Stress–strain curves of as-cast and aged Zr62 MGs. (c) Schematic diagram of the ultrasonic vibrational equipment. (d) Schematic diagram of the UV treatment procedure and photos of the samples at each step. (e) Stress versus time during UV loading. (f) Temperature versus time during UV loading.

suppl. figures S3 and S4. As can be observed from figure S4, the largest enthalpy change takes place with an amplitude of 35.5 μm (80%). Consequently, this amplitude was selected in this work.

The property evolution of the MGs treated under different UV conditions is presented in figure 2(a). The black curve of the as-cast sample serves as a reference, exhibiting a plastic strain of 9.6% and a yield strength of 1.547 GPa, while the T_g-10 h aged (abbreviated as T_g-10 h hereafter) MG displays zero plastic strain. In comparison, the UV-75J sample starts to exhibit a plastic strain of 4.2% and a yield strength of

1.43 GPa. When the UV energy increases to 100 J, the plasticity of the samples further increases to 14.5% and the yield strength increases to 1.68 GPa, even surpassing those of the as-cast samples. When the energy continues to increase, the plastic strain of the UV-125J sample decreases to 3.4%, and the yield strength decreases to 1.52 GPa. As a result, the best performance is observed in the UV-100J sample, exhibiting the plasticity superior to that of the as-cast sample by 50%. We conduct the mechanical property tests for each energy at least five times. Figure S5 in supplementary materials shows the replica data of the compression test for different energy
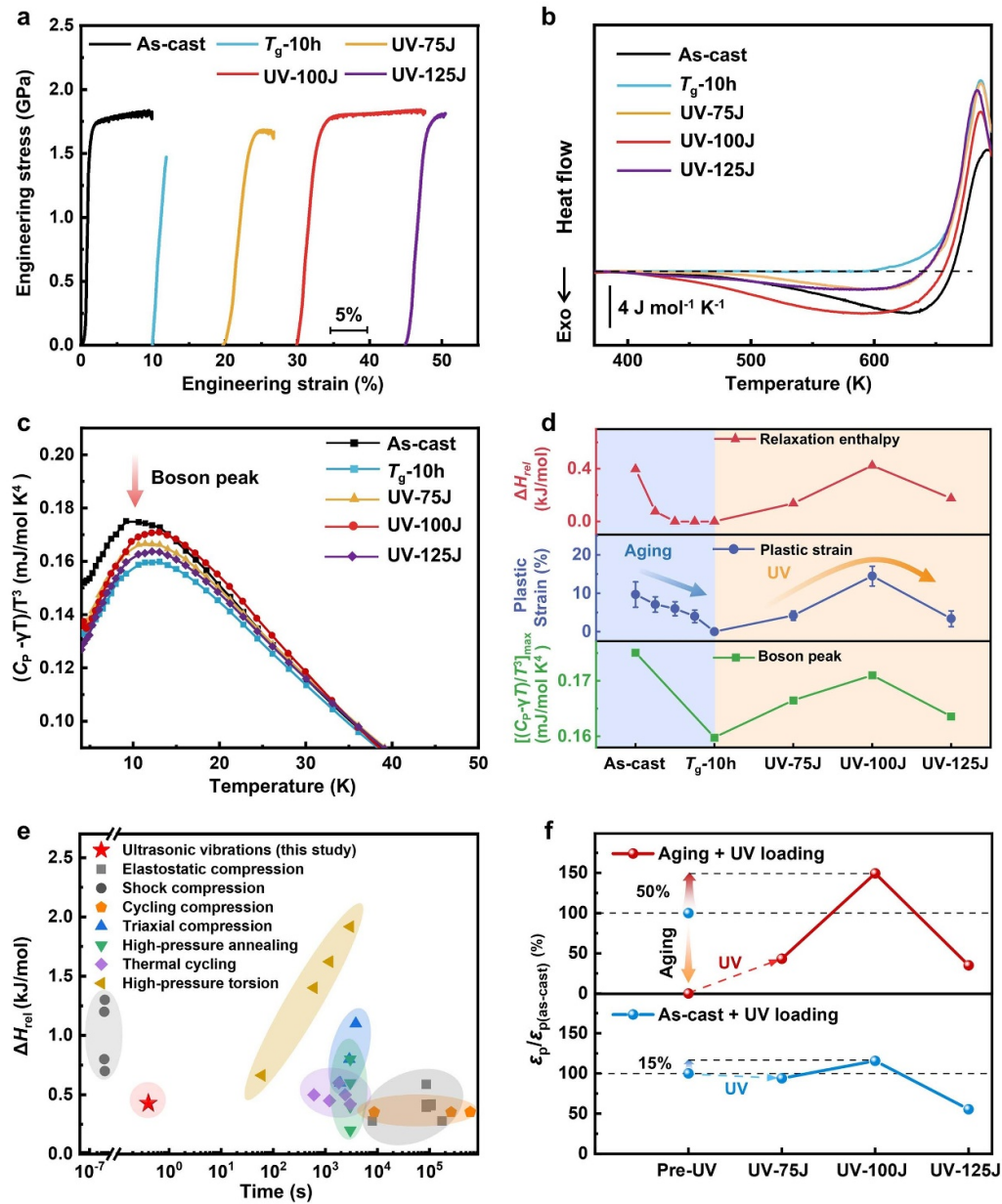
Figure 2. Property evolution of the samples undergoing different treatments. (a) Stress–strain curves of aged samples after UV loading. (b) DSC curves of the aged samples after UV loading. (c) $(C_p - \gamma T)/T^3$ versus temperature (T) for samples before and after UV loading. (d) Relaxation enthalpy, plastic strain and boson peak intensity of samples at the aging treatment and the UV treatment stages. (e) Excess relaxation enthalpy of MGs as a function of the time scale of various rejuvenation methods. It includes UV loading in this study, elastostatic compression [43], cycling compression [44], triaxial compression [20, 21], high-pressure annealing [45], thermal cycling [16, 46], high-pressure torsion [47], and shock compression [41]. (f) Performance variation of MGs subjected to UV treatment with different initial states (The *y*-axis represents the percentage relationship of plastic strain between differently treated samples and the as-cast sample).

values, and the corresponding margins of error are shown in suppl. table S1. These data confirm that the plasticity results are reproducible.

The DSC curves for the aged samples before and after the UV loading treatment (the sample is taken from a cross-section of one end of the cylinder) are shown in figure 2(b). After long-time annealing, the ΔH_{rel} decreases from 0.393 kJ mol^{-1} to 0 kJ mol^{-1}. However, when UV loading is applied to the well-annealed sample, the ΔH_{rel} begins to recover. As the

UV energy increases, the ΔH_{rel} recovers to 0.104 kJ mol^{-1} for UV-75J and 0.075 kJ mol^{-1} for UV-125J. Specifically, the ΔH_{rel} recovers to 0.510 kJ mol^{-1} for UV-100J, exceeding that of the as-cast sample. Under UV loading, rejuvenation and aging compete with each other, and excessive energy can lead to the aging of MGs [26, 37, 38]. Therefore, there is an optimal energy threshold for UV-induced rejuvenation. The hardness and modulus are shown in suppl. figures S6 and S7. It is found that aging increases the hardness and modulus,

while UV loading leads to a decrease in them. This tendency is consistent with the influence of aging and UV treatment on other properties.

The state of MGs is further characterized by the low temperature heat capacity. At terahertz frequencies, glasses can display an excess of vibrational modes over the Debye level, forming a vibrational anomaly called BP [39]. These additional vibrations enhance the low-temperature specific heat capacity C_p, and the BP appears as a hump in the plot of C_p/T^3 versus T at the temperature of $\sim$10 K. For MGs, the electronic part Cele p of the low-temperature C_p is known to be equal to γT, where γ is the electronic specific heat coefficient [40, 41]. The Cele p is subtracted to make the BP more pronounced. Then, we plotted the curve of $(C_p-\gamma T)/T^3$ vs. T in figure 2(c), where the BP is clearly visible at $\sim$10 K. It is noted that the BP intensity shows a positive correlation with the ΔH_{rel} change in figure 2(b) [42]. The BP value of the as-cast sample is 0.1751 mJ (mol^{-1} K^{-4}), and it decreases to 0.1598 mJ (mol^{-1} K^{-4}) at the T_g-10 h sample. After UV treatment, the BP intensities are all higher than that of the T_g-10 h sample. Among processed samples, the BP intensity of the UV-100J sample is highest and close to the as-cast sample.

The property evolution of aged samples before and after UV loading treatment is summarized in figure 2(d), with the corresponding mechanical properties, relaxation enthalpy, and BP intensity listed in suppl. table S1. During the annealing treatment stage, the ΔH_{rel} decreases to 0 kJ mol^{-1} at 1 h, while the plastic strain gradually decreases to 0% until 10 h. During the UV treatment stage, the ΔH_{rel}, plastic strain and BP intensity all initially increase, reaching maximum values at 100 J, and decrease with further increasing the applied UV energy. In comparison, the UV-100J sample exhibits higher yield stress, larger plasticity and higher relaxation enthalpy than the as-cast one, while displaying a smaller BP intensity.

An extensive comparison between this study and previous methods (treating bulk specimens) is summarized in figure 2(e) by plotting the ΔH_{rel} as a function of time. The aging reversal process is achieved within an exceptionally short time scale of just 0.5 s in this work. This time scale is significantly shorter than that of currently available rejuvenation techniques, being at least 2 orders of magnitude faster. While the shock compression method is rapid, it can cause significant destructive effects on the samples. Therefore, it is evident that UV loading is a rapid and effective way to reverse the aging process and facilitate mechanical recovery in aged BMG.

The above results demonstrate that the samples subjected to UV loading after aging display larger plasticity than the as-cast counterparts. It indicates that rejuvenation does not signify a return to the initial state but rather a transition to a new, higher-energy state. This observation leads to an interesting question: whether superior plasticity can be achieved through UV loading by selecting different initial states.

To explore this question, we examined the plasticity of as-cast samples after UV loading. Figure 2(f) presents the performance variation of MGs subjected to UV treatment with different initial states. After UV treatment, the plasticity of the aged sample increased from 0 to 14.5%, which is approximately a 50% increase compared to the as-cast sample.

When the as-cast sample was subjected to 100 J of ultrasonic energy, its plasticity increased by approximately 15% compared to the as-cast sample (The mechanical properties of the 'as-cast +UV loading' sample are presented in the suppl. figure S8). As a result, the optimal performance is observed in the sample undergoing UV loading after aging. Notably, similar enhancement in catalysis property has also been found in Pt-based MGs treated by post-aging UV loading, which will be detailed in forthcoming publications. Therefore, we propose a 'aging-assisted UV loading' approach that is a viable strategy to enhance the properties of the MGs.

To explore the mechanism of the plasticity enhancement through the aging-assisted UV loading method, we studied the evolution of the microstructure after each process. Figure 3 shows the SEM images and schematic diagram of the Zr62 rods after compression tests. A high density of multiple shear bands (SBs) marked by golden arrows appears on the side surface of the as-cast rod (figure 3(a)). These SBs branch and interact with one another (marked by the golden circle in figure 3(a)), and the interactions prevent the rapid expansion of the main SBs along a single direction. The SEM image of the fracture surface exhibits vein-like patterns and dimples which are typical features of the fracture surface in highly plastic MGs, as shown in figure 3(b). Similar results are observed in other MGs with good compression plasticity [13, 48]. A schematic diagram of dimples is shown in figure 3(c). In figures 3(d)–(f) of the T_g-10 h aged sample, SBs and dimples disappear, and smooth regions appear (marked by orange circles in figures 3(e) and (f)), which is consistent with the disappearance of plasticity in the well-aged sample. When the aged samples undergo the UV loading, the SBs and vein-like patterns reappear (figures 3(g)–(o)). It is noted that the UV-100 J sample displays the densest SBs in figure 3(k), consistent with its largest plasticity among all the samples.

To further investigate the structural differences associated with the aged and rejuvenated samples, high-energy x-ray diffraction experiment was conducted. The obtained structure factors S(Q) of the samples undergoing different treatments are shown in figure 4(a). The first two peaks were enlarged for a better distinction (see figures 4(b) and (c)), which qualitatively reflect the medium-range order (MRO) of the atomic structure of glasses [49]. A sharpening of these two peaks can be seen for the aged sample, while a downward peak shift is discernible for the UV-100J sample. The sharpening of the peaks has been widely observed in aged MGs [50], being attributed to the relaxation-generated more ordered configuration of the structure. In contrast, the decreased peak height indicates that the UV treatment pulls the aged structure back to a more disordered state.

The short-range order (SRO) as well as short- to medium-range information can be extracted from the atomic pair distribution functions (PDFs) G(r), which quantify the probability of atomic pairs occurring at specific intervals from a central atom. The G(r) of samples undergoing different treatments are shown in figure 4(d). For better observation, the first four peaks are enlarged and denoted as r1, r2, r3, r4 in figures 4(e)–(h), respectively. The peak heights of the r1, r3, r4 in the well-aged sample exhibit a significant increase compared to those in the
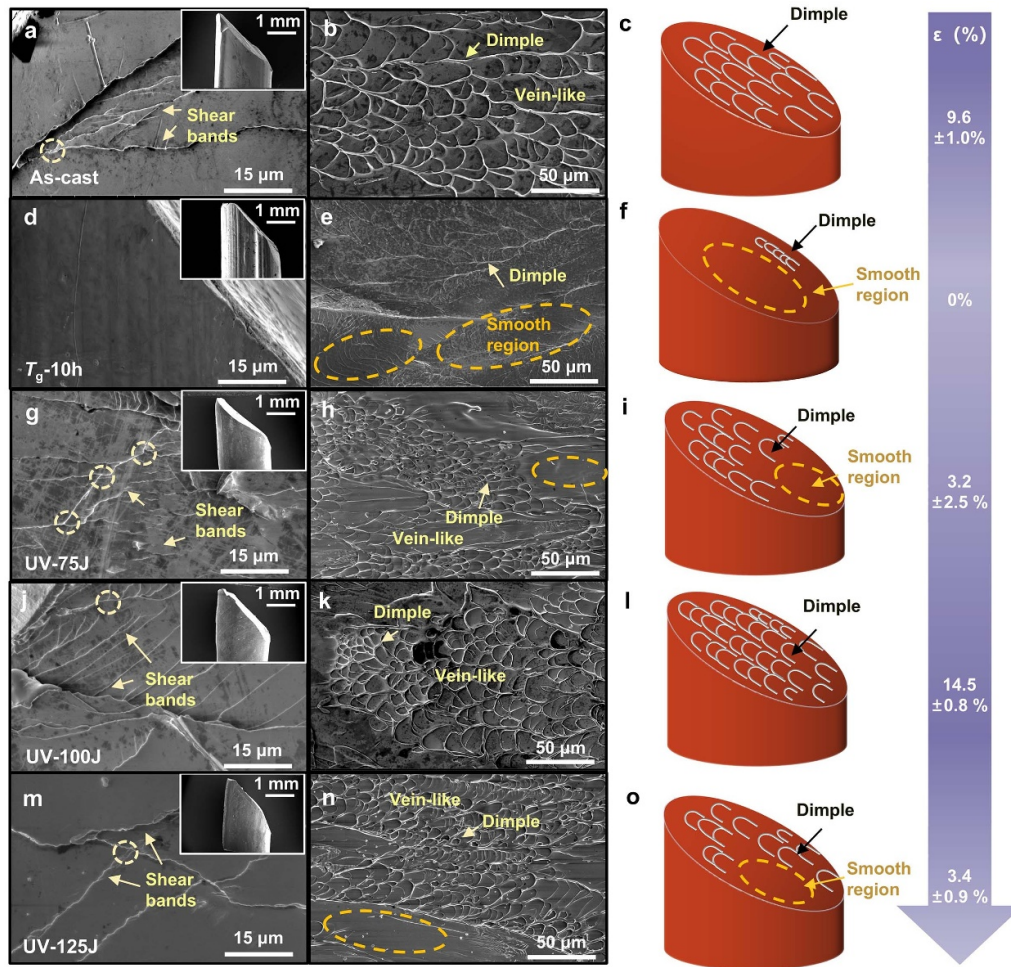
Figure 3. SEM images of the sides and fracture surfaces of samples under different treatments. As-cast sample: (a) side, (b) fracture surface and (c) Schematic diagram of dimples. T_g-10 h sample: (d) side, (e) fracture surface and (f) Schematic diagram of dimples. UV-75J sample: (g) side, (h) fracture surface and (i) Schematic diagram of dimples. UV-100J sample: (j) side, (k) fracture surface and (l) Schematic diagram of dimples. UV-125J sample: (m) side, (n) fracture surface and (o) Schematic diagram of dimples. SBs and vein-like patterns (dimples) are denoted by golden arrows. Intersection points of SBs are marked by golden circles. Smooth regions are highlighted by orange circles. The purple arrow shows the plastic change of different treated samples.

as-cast sample. This is a typical signature of structural relaxation in glasses [51], indicating a tighter local structure. In comparison, for the UV-100J sample, these three peaks decrease and lie between the aged and as-cast samples. The change in peak area can quantify the coordinate number of different atomic shells, and the change in peak height can indicate changes in the degree of structural disorder. To gain insights into the coordination number of samples undergoing different treatments, we carefully compared the nearest-neighbor peak r1 of $G(r)$. We conducted subpeak analysis and integration in suppl. figures S9(a)–(c) [52, 53], and found that the trends in peak area and peak height are consistent, as illustrated in suppl. figure S9(d). It indicates that the material becomes more ordered after aging, but becomes disordered again after post-aging UV loading.

The decrease in r1 peak area and height for the UV-100J sample evidences a less coordinated SRO. This is a signature of the rejuvenation of MGs, concurring well with reported results [53]. The structural rejuvenation extends to at least 4 atomic shells, as illustrated in figures 4(e)–(h). However, the second peak r2 of UV-100J sample shows no declination, instead a slight increment. This may originate from the different effect on the atomic structure between ultrasonic sound and temperature. The peak change indicates the UV treatment causes a change in medium-range order, but the path under UV loading is not a simple return to the original aging path. A more detailed study on the PDFs of UV loading is required in the future.

The above results exhibit that the rejuvenation effect takes place after UV loading, which is similar to that of La-based MGs in the previous work [31]. However, there is a notable distinction between La-based and Zr-based MGs in their response to UVs. La-based MGs exhibit rejuvenation accompanied by large ultrasonic-vibration-induced plasticity of 80% [31], whereas Zr-based MGs demonstrate rejuvenation with only a minute deformation of 1%, as shown in
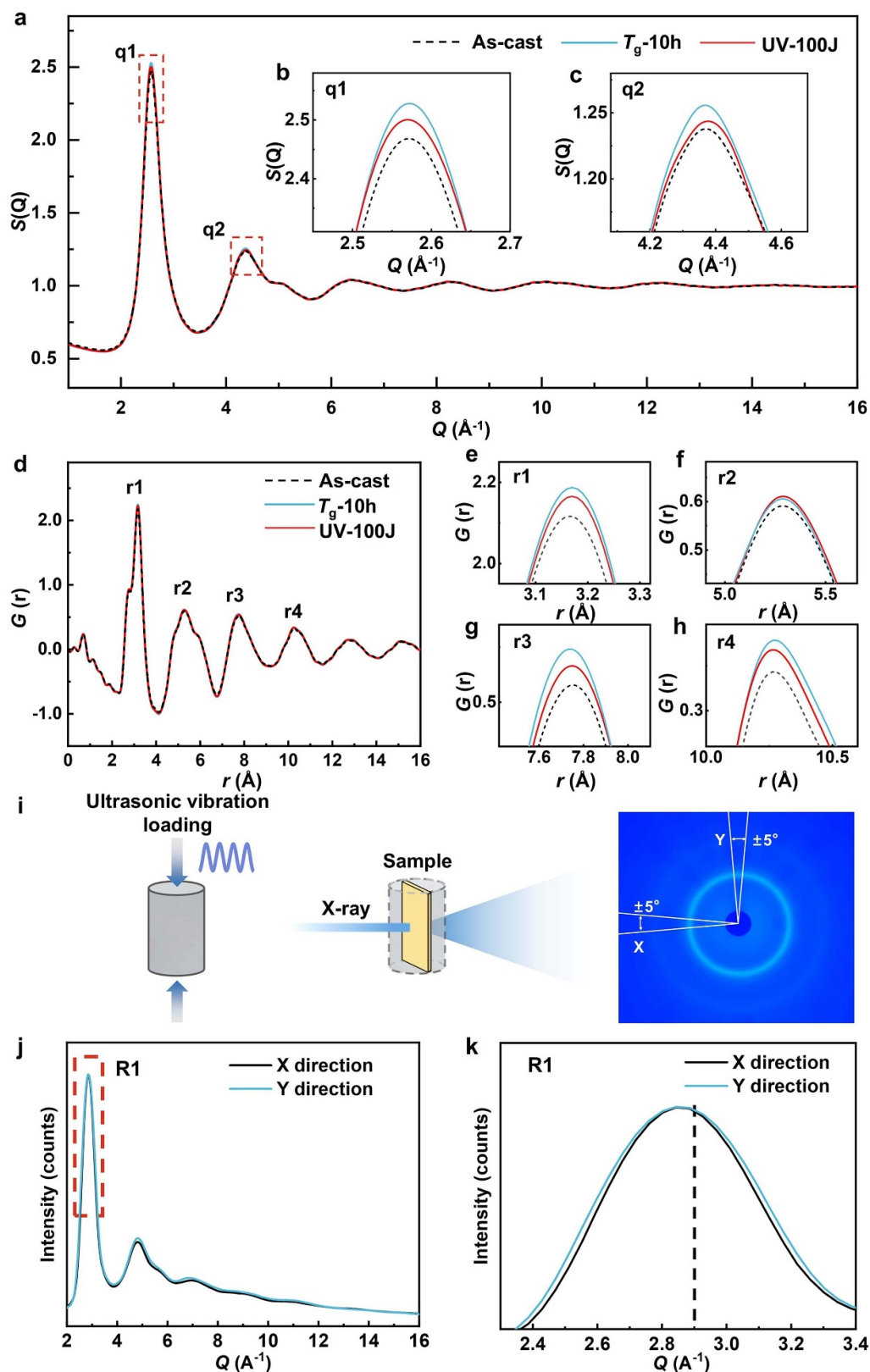
Figure 4. PDFs and the atomic structures of samples undergoing different treatments. (a) Synchrotron x-ray diffraction results of samples in Q-space. (b) Enlarged first diffraction peak in the red box. (c) Enlarged second diffraction peak in the red box. (d) Synchrotron x-ray diffraction results of samples in real space. (e) Enlarged image of the first diffraction peak (r1). (f) Enlarged image of the second diffraction peak (r2). (g) Enlarged image of the third diffraction peak (r3). (h) Enlarged image of the fourth diffraction peak (r4). (i) Schematic of structural anisotropy detection and two-dimensional diffraction patterns of UV-100J samples. The horizontal direction is designated as the *X* direction, and the vertical direction is designated as the *Y* direction. (j) Diffraction patterns integrated over the *X* and *Y* directions with a range of $\pm 5°$. (k) Enlarged image of the diffraction peak (R1).
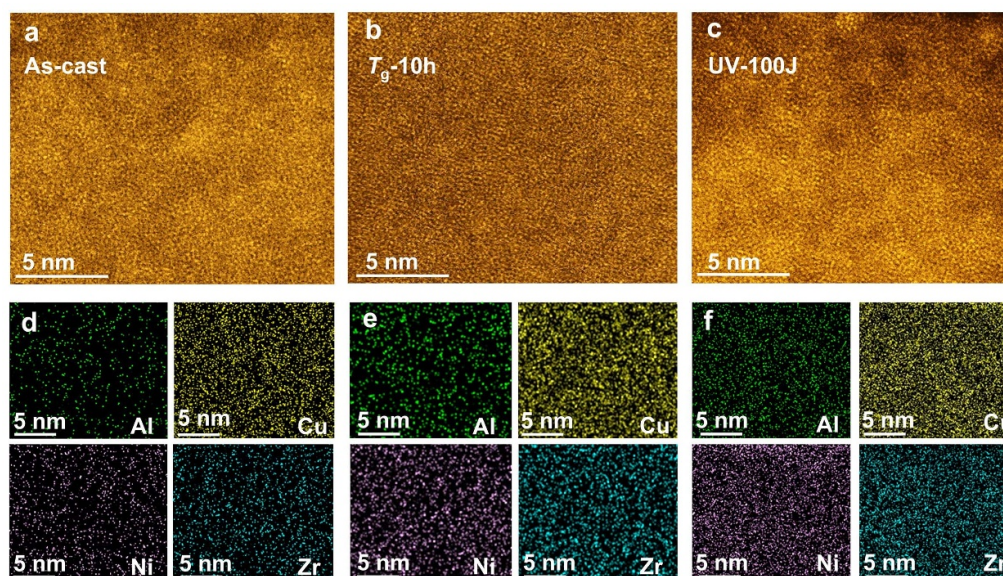
Figure 5. Atomic structure and corresponding elemental distribution of the samples undergoing different treatments. (a)–(c) HAADF-STEM images of the (a) as-cast, (b) T_g-10 h and (c) UV-100J samples. (d)–(f) Corresponding EDS chemical mappings for the (d) as-cast, (e) T_g-10 h and (f) UV-100J samples.

suppl. figure S10. Consequently, the origin of the rejuvenation effect, whether due to UVs or plastic deformation, remains an unresolved question.

In order to solve this question, we have studied the structural anisotropy change of the UV-100J sample, which was explored by high-energy synchrotron radiation x-ray anisotropy testing as proposed by Dmowski *et al* [54]. Figure 4(a) is a schematic illustration for structural anisotropy detection. Figure 4(b) shows the 2D diffraction pattern obtained from the anisotropy test, and no obvious structural anisotropy is observed. To better contrast the differences in the diffraction pattern along the *X* and *Y* directions, we performed integration over these directions (with a range of $\pm 5°$) to obtain two curves, as shown in figure 4(c). The inset in figure 4(c) is an enlargement of the diffraction peak within the red box, where the consistent peak positions indicate that the structural anisotropy of the UV-100J sample is negligible. In MGs, significant structural anisotropy appears during creep and plastic deformation under anisotropic loads such as uniaxial compression or tension, which is caused by localized plastic deformation leading to bond opening and closing [55, 56]. In contrast, negligible structural anisotropy was observed in UV-treated samples in this work. Therefore, this result indicates that the structural rejuvenation effect is not attributed to plastic deformation, but induced by UVs.

To further confirm the origin of rejuvenation in the UV-treated sample, we performed experiments to detect the possible sub-T_g exothermic peak in Zr-based MGs with the same plasticity level under conventional compression. As shown in suppl. figures S11(a), (c) and (e), T_g-3 h samples demonstrate a plasticity of 0.3%, 0.7% and 1% under conventional compression test, respectively. It is noted that none of these deformed samples exhibit a sub-T_g exothermic peak in the DSC curves shown in suppl. figures S11(b), (d) and (f). These results also indicate that the rejuvenation is not due to plastic deformation, but rather caused by UVs.

It is well known that the plasticity of MGs is related to their spatial heterogeneity in the nanoscale domains [57]. Scanning TEM (STEM) analysis with a high-angle annular dark-field (HAADF) detector was performed to characterize the local atomic structure. In figure 5(a), the HAADF-STEM image of the as-cast sample presents obvious structural heterogeneity with dark regions sizes of $\sim$2.5 nm [58–61]. In comparison, the structure of the well-annealed MG is more uniform and dark regions become indistinguishable in figure 5(b). Strikingly, the structural heterogeneity reappears in the UV-100J sample, as shown in figure 5(c). No detectable composition difference between the dark and bright domains is found in figures 5(d)–(f), suggesting all the samples are compositionally homogenous. Therefore, these results reveal that the structural heterogeneity after UV loading is not accompanied by the compositional heterogeneity.

As shown in figure 2(b), compared to the as-cast sample, the DSC curve of the UV-100J sample shows an earlier onset of enthalpy relaxation, suggesting a softening effect with a lower activation barrier for structural relaxation. In comparison, the UV-treated sample in figure 2(c) exhibits a rightward shift in the position of the BP (higher frequency) compared to the as-cast sample. This indicates a hardening effect whereby the population of defect-like excitations increases after UV treatment, while these defects require higher activation energy for excitation. Thus, there is an apparent contradiction between the softening effect in DSC data and the hardening effect in BP. This intriguing contradiction can be well explained by the framework of the 'anti-free volume defects' proposed by Egami [62].

From a microscopic perspective, the microstructure of MGs can be conceptualized as structural defects randomly
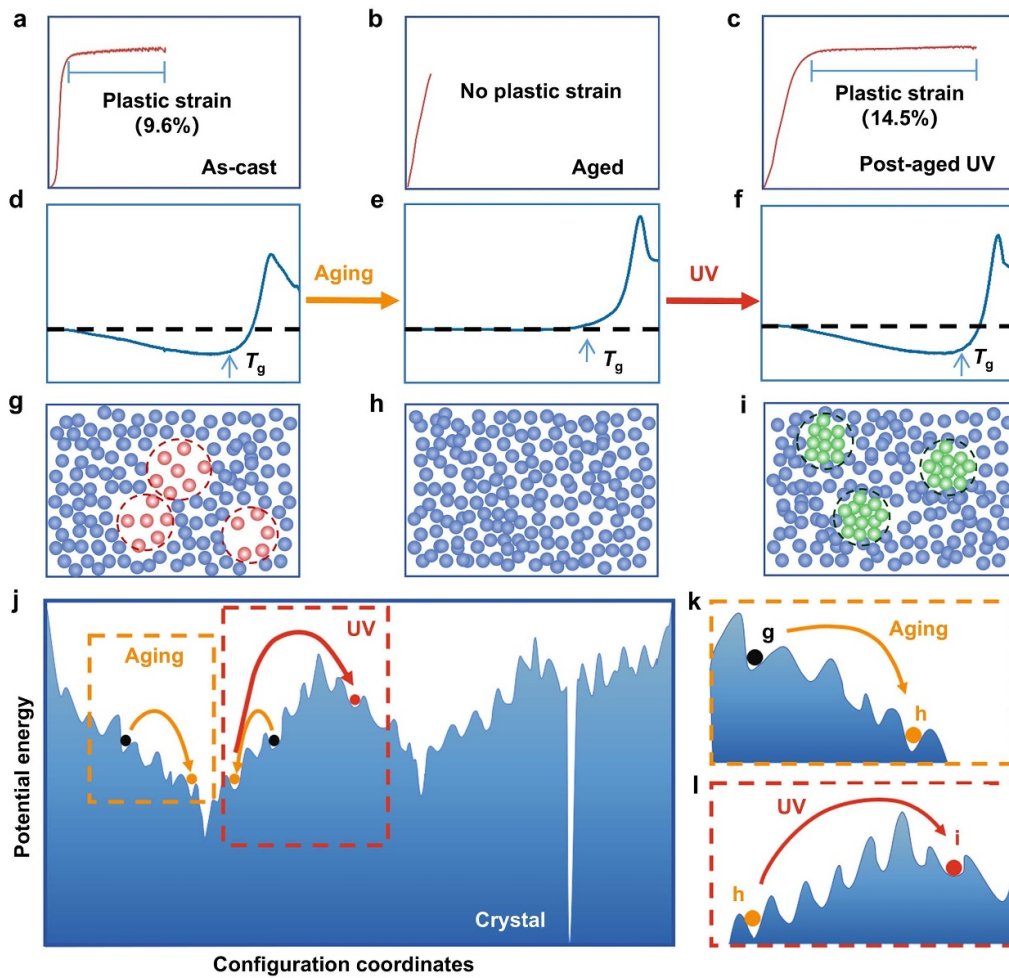
Figure 6. Aging process and UV-induced reverse aging process interpreted through a potential energy landscape. (a)–(c) Stress–strain curves. (d)–(f) DSC curves and (g)–(i) Schematic microstructures of MGs under different treatments. The red, green and blue atomic regions represent the free volume defects, anti-free volume defects and solid matrix, respectively. (j)–(l) Schematic diagrams of the PEL of MGs. (k) The change in the energy state of MGs during aging (orange box). (l) The change in the energy state of aged MGs during UV loading (red box).

distributed in a solid matrix [63, 64]. The structural defects are generally considered to be regions of low density with free volumes (also known as the 'liquid-like region' or 'soft zone'). However, there are also another type of defects with higher density and higher energy, which are the anti-free volume defects [45, 62]. Free volume defects are loosely structured defects characterized by a high-energy state, low density, and low modulus. In contrast, anti-free volume defects, also referred to as negative flow units, are tightly structured defects characterized by a high-energy state, high density, and high modulus [45, 62].

In the context of the anti-free volume defects, the apparent contradiction can be properly interpreted. The anti-free volume defects have a higher structural density than free volume defects, so their activation frequency is higher than that of free volume defects, corresponding to the rightward shift in BP position. Conversely, as high-density structural defects, anti-free volume defects are more sensitive to thermal expansion. During heating, these defects are activated earlier due to their higher density, leading to the leftward shift in the

exothermic peak position. Consequently, this apparent contradiction indicates that UV loading introduces unusual anti-free volume defects into the UV-treated sample.

These anti-free volume defects can also well explain the enhanced plasticity in UV-treated aged samples. There are abundant free volume defects in as-cast samples. The anti-free volume defects introduced by UV treatment may annihilate the free volume defects, thereby reduce the net defect density and limit plasticity enhancement. In stark contrast, aging reduced free volume defects in aged samples, leading to a homogenous densified structure. The subsequent UV treatment introduces anti-free volume defects, which act as stress concentrators to facilitate SB nucleation, leading to a strong plasticity enhancement.

We then attempted to explain the property evolution based on the schematic diagram of the structure defects and energy landscape. The plastic deformation changes after aging and UV loading are shown in figures 6(a)–(c). Figures 6(d)–(f) exhibit the exothermic relaxation enthalpy changes after aging and UV loading. The free volume, anti-free volume defects

and the solid matrix are represented by red, green, and blue atoms, respectively, in figures 6(g)–(i). After a certain period of aging, free volume defects are eliminated, and the system relaxes to a more homogeneous state, as shown in figure 6(h). Consequently, no plasticity is observed in figure 6(b), and the sub-T_g exothermic peak disappears in figure 6(e). After UV loading, new anti-free volume defects are introduced, which corresponds to the reappearance of the plastic deformation and the sub-T_g exothermic peak in figures 6(c) and (f).

To explain the energy evolution of the aged sample under UV loading, we also established a potential energy landscape (PEL) in figures 6(j)–(l), in which several potential energy minima/mega basins between different configurations are illustrated. The deepest energy minimum on the PEL corresponds to a stable crystalline phase, while other energy minima represent metastable glassy states [31]. As-cast MGs are formed by the rapid cooling of the melt, leaving some energy trapped in the glass, which corresponds to the formation of free volume in the microstructure. During aging, the as-cast sample tends to move towards a more stable state. When the aging time is long enough, the energy state of the aged MGs becomes relatively low in figure 6(j), so soft zones are annihilated in figure 6(h), which is responsible for the disappearance of the exothermic peak in figure 6(e). Intriguingly, UV loading can inspire the state of the well-aged samples to a higher energy level as illustrated in figure 6(l), corresponding to the anti-free volume defects in figure 6(i). Simultaneously, this process is accompanied by the recovery of plasticity in figure 6(c) and the emergence of an exothermic peak in figure 6(f).

4. Conclusions

In summary, we reported that UV loading can make outstanding plasticity recovery of the aged MGs in a short time. The well-aged samples have completely lost their compressive plasticity, while post-aging UV treatment results in even better plasticity than that of the as-cast ones. The significant plasticity recovery is attributed to the rebound to a higher energy state induced by UV treatment, which is evidenced by the strong restoration of the structural enthalpy change and BP intensity, as well as the more disordered structure revealed by the pair distribution functions. Negligible structural anisotropy indicates that the rejuvenation is induced by UVs, instead of plastic deformation. The conceptual framework of anti-free volume defects offers a compelling explanation for these experimental observations. Accordingly, we proposed a method of 'aging-assisted UV loading' that can improve the performance of MGs. This work offers an alternative approach to heal and repair degenerate glasses and further helps to unveil the mechanism behind the structural evolution of MGs.

5. Future perspectives

MGs show great prospects both in fundamental research and engineering applications due to their unique amorphous structure and excellent properties. However, the aging of glassy materials is an inevitable process, ultimately leading to property degradation. This work demonstrates that aging is no longer a detrimental process, but an essential prerequisite to facilitate the following UV treatment to achieve even better plasticity than that of as-cast MGs. This finding breaks through the traditional perception of aging effects and opens up a new research direction for the property modulation of MG.

From a theoretical standpoint, the anti-free volume defect framework offers a compelling explanation for our experimental observations. However, the direct experimental evidence for these defects remains elusive, representing a critical gap in our understanding of their structural manifestation. Future studies are needed to obtain direct evidence for the formation of anti-free volume defects through molecular dynamics simulations or positron annihilation spectroscopy. Such investigations will not only validate the anti-free volume defects, but also offer critical insights into the atomic-scale mechanisms governing defect-mediated plasticity in MGs.

From a broader perspective, this strategy offers new possibilities for the functional application of amorphous alloys and may potentially be extended to multiple functional material fields, such as catalytic performance modulation (in Pd-based or Pt-based MGs) and soft magnetic property optimization (in Fe-based MGs), holding significant scientific and application value. Moreover, the relationship between the energy threshold exhibited in this work and the amorphous composition, as well as the long-term stability of the samples after ultrasonic treatment, still warrant further investigation.

Acknowledgments

Conflict of interest

The authors declare no competing interests.

Author contributions

S.R. and J.M. conceived the work. J.M., X.L. and S.R. supervised the work. J.C. conducted the ultrasonic vibrations experiments. J.C. and L.Z. performed the SEM. X.W., X.Z., S.S. and J.X. conducted the reference investigation. J.C., J.Z., Z.C. and

Y.Z. carried out TEM observation, XRD, DSC and mechanical properties test. J.D., Z.L., D.M. and K.Y. conducted the HE-x-ray experiment and analyzed the data. J.C., J.D., S.R. and J.M. wrote the manuscript. All authors contributed to the discussion and analyzed the results.

ORCID iD

Jiang Ma ⓘ 0000-0003-0234-3210

References

[1] Struik L C E 1978 *Physical Aging in Amorphous Polymers and Other Materials* (Citeseer)

[2] Liang S, Zhu F, Wang Y-J, Pineda E, Wada T, Kato H and Qiao J 2024 On the kinetics of structural evolution in metallic glasses *Int. J. Eng. Sci.* **205** 104146

[3] Liang S, Zhang L, Wang Y, Wang B, Pelletier J and Qiao J 2024 A model on the coupling between cyclic fatigue and microstructure evolution in a metallic glass *Int. J. Fatigue* **187** 108446

[4] Xing G, Hao Q, Zhu F, Wang Y-J, Yang Y, Kato H, Pineda E, Lan S and Qiao J 2024 Correlating dynamic relaxation and viscoelasticity in metallic glasses *Sci. China* **67** 256111

[5] Berthier L and Biroli G 2011 Theoretical perspective on the glass transition and amorphous materials *Rev. Mod. Phys.* **83** 587

[6] Ediger M D, Angell C A and Nagel S R 1996 Supercooled liquids and glasses *J. Phys. Chem.* **100** 13200–12

[7] Zhou J *et al* 2023 Ultrahigh permeability at high frequencies via a magnetic-heterogeneous nanocrystallization mechanism in an iron-based amorphous alloy *Adv. Mater.* **35** 2304490

[8] Liu Y, Wang G, Pan M, Yu P, Zhao D and Wang W 2007 Deformation behaviors and mechanism of Ni–Co–Nb–Ta bulk metallic glasses with high strength and plasticity *J. Mater. Res.* **22** 869–75

[9] Wang W H 2012 The elastic properties, elastic models and elastic perspectives of metallic glasses *Prog. Mater. Sci.* **57** 487–656

[10] Demetriou M D, Launey M E, Garrett G, Schramm J P, Hofmann D C, Johnson W L and Ritchie R O 2011 A damage-tolerant glass *Nat. Mater.* **10** 123–8

[11] Sarac B and Schroers J 2013 Designing tensile ductility in metallic glasses *Nat. Commun.* **4** 2158

[12] Wang Q, Yang Y, Jiang H, Liu C, Ruan H and Lu J 2014 Superior tensile ductility in bulk metallic glass with gradient amorphous structure *Sci. Rep.* **4** 4757

[13] Liu Y H, Wang G, Wang R J, Zhao D Q, Pan M X and Wang W H 2007 Super plastic bulk metallic glasses at room temperature *Science* **315** 1385–8

[14] Khonik V, Afonin G, Vinogradov A Y, Tsyplakov A and Tyutin S 2016 Crossover and normal structural relaxation in naturally aged glassy $Pd_{40}Cu_{30}Ni_{10}P_{20}$ *Intermetallics* **74** 53–59

[15] Ross P, Küchemann S, Derlet P M, Yu H, Arnold W, Liaw P, Samwer K and Maaß R 2017 Linking macroscopic rejuvenation to nano-elastic fluctuations in a metallic glass *Acta Mater.* **138** 111–8

[16] Ketov S *et al* 2015 Rejuvenation of metallic glasses by non-affine thermal strain *Nature* **524** 200–3

[17] Sun K *et al* 2020 Structural rejuvenation and relaxation of a metallic glass induced by ion irradiation *Scr. Mater.* **180** 34–39

[18] Dong J, Feng Y-H, Huan Y, Yi J, Wang W-H, Bai H-Y and Sun B-A 2020 Rejuvenation in hot-drawn micrometer metallic glassy wires *Chin. Phys. Lett.* **37** 017103

[19] Dong J, Huan Y, Huang B, Yi J, Liu Y, Sun B, Wang W and Bai H 2021 Unusually thick shear-softening surface of micrometer-size metallic glasses *Innovation* **2** 100106

[20] Pan J, Ivanov Y P, Zhou W H, Li Y and Greer A L 2020 Strain-hardening and suppression of shear-banding in rejuvenated bulk metallic glass *Nature* **578** 559–62

[21] Pan J, Wang Y X, Guo Q, Zhang D, Greer A L and Li Y 2018 Extreme rejuvenation and softening in a bulk metallic glass *Nat. Commun.* **9** 560

[22] Zhang S, Shi B, Wang J, Xu Y and Jin P 2021 Rejuvenation of a naturally aged bulk metallic glass by elastostatic loading *Mater. Sci. Eng. A* **806** 140843

[23] Huang Z, Fu J, Li X, Wen W, Lin H, Lou Y, Luo F, Zhang Z, Liang X and Ma J 2021 Ultrasonic-assisted rapid cold welding of bulk metallic glasses *Sci. China Mater.* **65** 255–62

[24] Li X *et al* 2020 Ultrasonic plasticity of metallic glass near room temperature *Appl. Mater. Today* **21** 100866

[25] Ma J *et al* 2019 Fast surface dynamics enabled cold joining of metallic glasses *Sci. Adv.* **5** eaax7256

[26] Li L *et al* 2023 Joining of metallic glasses in liquid via ultrasonic vibrations *Nat. Commun.* **14** 6305

[27] Li X *et al* 2024 Ultrasonic vibration enabled under-liquid forming of metallic glasses *Sci. Bull.* **69** 163–6

[28] Chang C, Zhang H, Zhao R, Li F, Luo P, Li M and Bai H 2022 Liquid-like atoms in dense-packed solid glasses *Nat. Mater.* **21** 1240–5

[29] Li W, Zuo X, Liu R, Pang C, Jin F, Zhu W and Yuan C 2024 Multi-scale defects activation in $Gd_{18.33}Tb_{18.33}Dy_{18.34}Co_{17.5}Al_{27.5}$ high-entropy metallic glasses revealed by nanoindentation *Int. J. Plast.* **174** 103893

[30] Li W *et al* 2025 Manipulating defects in metallic glasses via ultrasonic treatment *Int. J. Mech. Sci.* **287** 109960

[31] Chen Z *et al* 2024 Plasticity and rejuvenation of aged metallic glasses by ultrasonic vibrations *J. Mater. Sci. Technol.* **181** 231–9

[32] Zhou Z, Peng H and Yu H 2019 Structural origin for vibration-induced accelerated aging and rejuvenation in metallic glasses *J. Chem. Phys.* **150** 204507

[33] Yang K, Dong Z-H, Zhou C-Y, Zhao Z-L, Liang D-X, Cao S-C and Li A-G 2024 Ultrahard x-ray multifunctional application beamline at the SSRF *Nucl. Sci. Tech.* **35** 98

[34] Toby B H and Von Dreele R B 2013 GSAS-II: the genesis of a modern open-source all purpose crystallography software package *J. Appl. Crystallogr.* **46** 544–9

[35] Juhás P, Davis T, Farrow C L and Billinge S J 2013 PDFgetX3: a rapid and highly automatable program for processing powder diffraction data into total scattering pair distribution functions *J. Appl. Crystallogr.* **46** 560–6

[36] Zhao R, Jiang H, Luo P, Shen L, Wen P, Sun Y, Bai H and Wang W 2020 Reversible and irreversible β-relaxations in metallic glasses *Phys. Rev. B* **101** 094203

[37] Zhu L, Li L, Huang J, Zhang H, Wang W, Chen J, Liu J and Ma J 2024 Corrosion resistance enhancement of bulk metallic glass through ultrasonic vibrations *J. Non-Cryst. Solids* **646** 123223

[38] De Gennes P-G 2000 Tapping of granular packs: a model based on local two-level systems *J. Colloid Interface Sci.* **226** 1–4

[39] Wang W H 2019 Dynamic relaxations and relaxation-property relationships in metallic glasses *Prog. Mater. Sci.* **106** 100561

[40] Ren S, Zong H-X, Tao X-F, Sun Y-H, Sun B-A, Xue D-Z, Ding X-D and Wang W-H 2021 Boson-peak-like anomaly

caused by transverse phonon softening in strain glass *Nat. Commun.* **12** 5755

[41] Ding G, Li C, Zaccone A, Wang W, Lei H, Jiang F, Ling Z and Jiang M 2019 Ultrafast extreme rejuvenation of metallic glasses by shock compression *Sci. Adv.* **5** eaaw6249

[42] Jiang M, Peterlechner M, Wang Y, Wang W, Jiang F, Dai L and Wilde G 2017 Universal structural softening in metallic glasses indicated by boson heat capacity peak *Appl. Phys. Lett.* **111** 261901

[43] Zhang M, Wang Y, Li F, Jiang S, Li M and Liu L 2017 Mechanical relaxation-to-rejuvenation transition in a Zr-based bulk metallic glass *Sci. Rep.* **7** 625

[44] Louzguine-Luzgin D, Zadorozhnyy V Y, Ketov S, Wang Z, Tsarkov A and Greer A 2017 On room-temperature quasi-elastic mechanical behaviour of bulk metallic glasses *Acta Mater.* **129** 343–51

[45] Wang C *et al* 2017 High stored energy of metallic glasses induced by high pressure *Appl. Phys. Lett.* **110** 111901

[46] Guo W, Yamada R and Saida J 2018 Rejuvenation and plasticization of metallic glass by deep cryogenic cycling treatment *Intermetallics* **93** 141–7

[47] Meng F, Tsuchiya K, Seiichiro S and Yokoyama Y 2012 Reversible transition of deformation mode by structural rejuvenation and relaxation in bulk metallic glass *Appl. Phys. Lett.* **101** 121914

[48] Zhu J, Gao W, Cheng S, Liu X, Yang X, Tian J, Ma J and Shen J 2022 Improving the glass forming ability and plasticity of ZrCuNiAlTi metallic glass by substituting Zr with Sc *J. Alloys Compd.* **909** 164679

[49] Dmowski W, Yokoyama Y, Chuang A, Ren Y, Umemoto M, Tsuchiya K, Inoue A and Egami T 2010 Structural rejuvenation in a bulk metallic glass induced by severe plastic deformation *Acta Mater.* **58** 429–38

[50] Liu Y, Fujita T, Aji D, Matsuura M and Chen M 2014 Structural origins of Johari-Goldstein relaxation in a metallic glass *Nat. Commun.* **5** 3238

[51] Küchemann S, Derlet P M, Liu C, Rosenthal D, Sparks G, Larson W S and Maaß R 2018 Energy storage in metallic glasses via flash annealing *Adv. Funct. Mater.* **28** 1805385

[52] Wei S, Wang X, Qiu K, Xu T, Cao Q, Ding S, Zhang D and Jiang J 2022 Short-range order controlling atomic dynamics in Y-based metallic glasses *Phys. Rev. B* **105** 054313

[53] Tong Y, Iwashita T, Dmowski W, Bei H, Yokoyama Y and Egami T 2015 Structural rejuvenation in bulk metallic glasses *Acta Mater.* **86** 240–6

[54] Dmowski W, Iwashita T, Chuang C-P, Almer J and Egami T 2010 Elastic heterogeneity in metallic glasses *Phys. Rev. Lett.* **105** 205502

[55] Dong J, Peng H, Wang H, Tong Y, Wang Y, Dmowski W, Egami T, Sun B, Wang W and Bai H 2023 Non-affine atomic rearrangement of glasses through stress-induced structural anisotropy *Nat. Phys.* **19** 1896–903

[56] Suzuki Y, Haimovich J and Egami T 1987 Bond-orientational anisotropy in metallic glasses observed by x-ray diffraction *Phys. Rev. B* **35** 2162

[57] Jiang J, Lu Z, Shen J, Wada T, Kato H and Chen M 2021 Decoupling between calorimetric and dynamical glass transitions in high-entropy metallic glasses *Nat. Commun.* **12** 3843

[58] Zhu F, Hirata A, Liu P, Song S, Tian Y, Han J, Fujita T and Chen M 2017 Correlation between local structure order and spatial heterogeneity in a metallic glass *Phys. Rev. Lett.* **119** 215501

[59] Liu Y, Wang D, Nakajima K, Zhang W, Hirata A, Nishi T, Inoue A and Chen M 2011 Characterization of nanoscale mechanical heterogeneity in a metallic glass by dynamic force microscopy *Phys. Rev. Lett.* **106** 125504

[60] Zhu F, Song S, Reddy K M, Hirata A and Chen M 2018 Spatial heterogeneity as the structure feature for structure–property relationship of metallic glasses *Nat. Commun.* **9** 3965

[61] Zhu F, Nguyen H, Song S, Aji D P B, Hirata A, Wang H, Nakajima K and Chen M 2016 Intrinsic correlation between β-relaxation and spatial heterogeneity in a metallic glass *Nat. Commun.* **7** 11516

[62] Egami T 2011 Atomic level stresses *Prog. Mater. Sci.* **56** 637–53

[63] Pei C, Chen S, Zhao T, Li M, Cui Z, Sun B, Hu S, Lan S, Hahn H and Feng T 2022 Nanostructured metallic glass in a highly upgraded energy state contributing to efficient catalytic performance *Adv. Mater.* **34** 2200850

[64] Tao K, Qiao J, He Q, Song K and Yang Y 2021 Revealing the structural heterogeneity of metallic glass: mechanical spectroscopy and nanoindentation experiments *Int. J. Mech. Sci.* **201** 106469